



Title	Thermofluid simulation of hydrogen isotopologue mixtures during the solidification process
Author(s)	Zhang, Jiaqi; Iwamoto, Akifumi; Shigemori, Keisuke et al.
Citation	Fusion Engineering and Design. 2025, 212, p. 114827
Version Type	VoR
URL	<a href="https://hdl.handle.net/11094/100582">https://hdl.handle.net/11094/100582</a>
rights	This article is licensed under a Creative Commons Attribution 4.0 International License.
Note	

*The University of Osaka Institutional Knowledge Archive : OUKA*

<https://ir.library.osaka-u.ac.jp/>

The University of Osaka



# Thermofluid simulation of hydrogen isotopologue mixtures during the solidification process

Jiaqi Zhang<sup>a,\*</sup>, Akifumi Iwamoto<sup>a,b</sup>, Keisuke Shigemori<sup>a</sup>, Masanori Hara<sup>c</sup>, Kohei Yamanoi<sup>a</sup>

<sup>a</sup> Institute of Laser Engineering, Osaka University, Osaka 5650871, Japan

<sup>b</sup> National Institute for Fusion Science, National Institutes of Natural Sciences, Gifu 509-5202, Japan

<sup>c</sup> Academic Assembly, University of Toyama, Toyama 9308555, Japan

## ARTICLE INFO

### Keywords:

Inertial confinement fusion target  
Hydrogen isotopologue  
Isotopologue fractionation  
Thermofluid simulation

## ABSTRACT

A typical inertial confinement fusion target comprises a central deuterium-tritium (D-T) gas surrounded by a solid D-T layer inside an outer ablator shell. However, because of the isotope effect, fractionation of the hydrogen isotopologues can occur during the solidification process. This inhomogeneity in the solid D-T layer may lead to a deterioration in the fusion reaction. Thus, effective methods are required to characterize isotopologue distribution and homogeneity in solid D-T layers. The distribution of isotopologues in a solid hydrogen mixture can be simulated numerically using computational fluid dynamics. In this study, thermofluid simulations of the mixture's solidification process were performed to investigate the mechanism behind component distribution and to analyze the factors affecting the homogeneity. A numerical simulation was conducted to model inhomogeneity formation during the solidification of hydrogen isotopologue mixtures in a 3D wedge-shaped cavity. The simulations revealed inhomogeneities in H<sub>2</sub>-D<sub>2</sub>, D<sub>2</sub>-T<sub>2</sub>, and D<sub>2</sub>-DT-T<sub>2</sub> mixtures during solidification. For an H<sub>2</sub>-D<sub>2</sub> mixture, the simulation showed good agreement with experimental results, validating the computational model. These simulation methods will be used for homogeneity analysis of the solid D-T layer in fuel pellets.

## 1. Introduction

Inertial confinement fusion (ICF) target designs are generally based on a spherical ablator capsule containing a solid deuterium-tritium (D-T) fuel layer surrounding a D-T vapor core at equilibrium vapor pressure (Fig. 1) [1]. Lasers, or heavy ion beams, illuminate and heat the ablator, causing its exterior to expand outward. The remaining interior implodes and compresses the D-T fuel until it reaches a high density. Near the peak compression [2], the D-T vapor forms a central "hot spot" where nuclear fusion reactions are initiated. The energy released from the fusion reaction heats the surrounding inner surface of the solid D-T fuel to the ignition temperature, initiating self-sustaining fusion reactions that propagate outward, continuing the burn [3]. The gas at the center provides a space to enable inward acceleration of the fuel and formation of the central hot spot [4]. Using a solid D-T layer as the main fuel enables compression to a higher fuel density, resulting in increased yield [5]. This target structure has been widely adopted since its proposal [6].

The target specifications for ICF are stringent. Nonuniformity

implosion of the fuel target can lead to a significant reduction in thermonuclear yield [7]. Generally, implosion nonuniformity is introduced by illuminating nonuniformity and imperfections in the target structure [8]. Sources of imperfections in the target structure include deviations from target sphericity, nonuniform layer thickness, and roughness at the layer surface [9]. In this study, we focused on the effect of the homogeneity in the solid D-T layer. Forming a solid D-T layer involves filling the evacuated capsule with D-T gas and condensing it uniformly on the inner surface of the capsule. However, during phase transition, isotopologue fractionation induces a change in the ratio of heavy to light isotopologues during the two phase changes [10]; namely, T, as a heavier hydrogen isotope, tends to enrich more rapidly in the solid phase during phase transitions, leading to a non-uniform distribution of D and T in the solid layer. During the cryogenic layering process, techniques such as decay heat and infrared radiation are used to repeatedly induce phase transitions in the D-T fuel, thereby causing the thickness of the solid D-T layer to gradually become uniform [11–15]. However, repeated phase transitions can intensify isotopologue fractionation in

\* Corresponding author.

E-mail address: [zhang-j@ile.osaka-u.ac.jp](mailto:zhang-j@ile.osaka-u.ac.jp) (J. Zhang).

<https://doi.org/10.1016/j.fusengdes.2025.114827>

Received 25 August 2024; Received in revised form 6 October 2024; Accepted 23 January 2025

Available online 1 February 2025

0920-3796/© 2025 The Authors. Published by Elsevier B.V. This is an open access article under the CC BY license (<http://creativecommons.org/licenses/by/4.0/>).

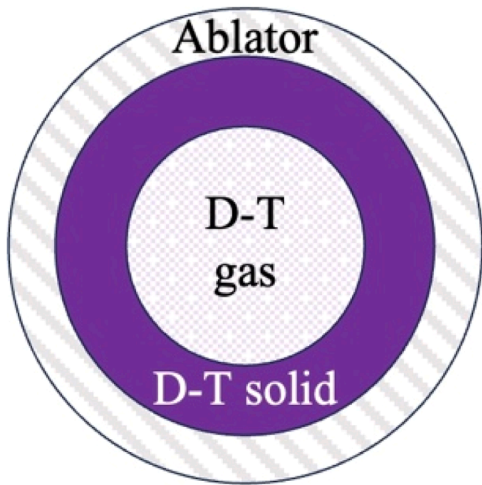


Fig. 1. Schematic of multilayer structure of D-T fuel target.

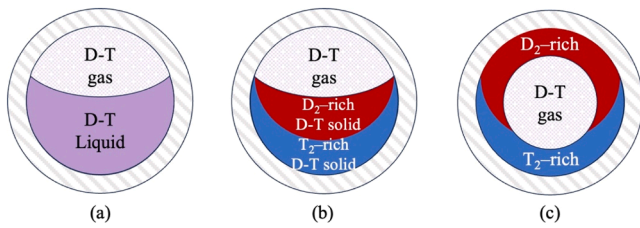


Fig. 2. Compositional deviation prediction of the solid D-T layer due to isotopologue fractionation. (a) Liquid D-T prior to solidifying. (b) As the temperature decreases, T solidifies first at the bottom. (c) Heating the target center results in the solid D-T sublimating before the top is sublimated.

the D-T layer (Fig. 2).

Inhomogeneity of the solid D-T layer may impact fusion reactions negatively: (1) The D-T vapor core is at the equilibrium vapor pressure; hence, as the  $D_2$  content increases on the inner surface of the solid layer, the  $D_2$  content in the gas also increases. The ignition temperature of the D-T reaction cannot reach the ignition conditions of the D-D reaction, and excess  $D_2$  hinders D-T fuel ignition. The solid D-T layer is the main fuel in the fusion reactions, and distortion of the fuel ratio leads to the degradation of D-T fusion. (2) Hydrodynamic instabilities that amplify nonuniformities related to non-sphericity during implosions reduce the thermonuclear yield. The non-uniform distribution of  $D_2$  and  $T_2$  affects

the spherical symmetry of the target density.

Isotopologue fractionation renders the preparation of a homogeneous solid D-T layer challenging. Therefore, an inspection method is required to characterize the isotopologue distribution and homogeneity of solid D-T through both numerical simulations and experiments. We demonstrated a method for characterizing solid D-T homogeneity by measuring the refractive-index distribution, as performed in Ref. [16]. In this study, computational fluid dynamics (CFD) was used to numerically simulate the compositional distribution of solid hydrogen isotopologue mixtures. A better understanding of the mechanisms of composition distribution during the solidification process, achieved through thermofluid simulations of the mixture, could provide a theoretical basis for controlling isotopologue fractionation. Additionally, it could predict the homogeneity of the solid D-T layer in the target using a 3D model.

## 2. Simulation settings

In the solid state, Hydrogen isotopologue mixtures are completely soluble in all proportions. The phase diagrams of H-D and D-T have been elucidated in Refs. [17] and [18]. Two main processes contribute to isotopologue fractionation: equilibrium and kinetic fractionation. In the experiment, the main cause of inhomogeneity in the solid hydrogen isotopologue mixture was non-equilibrium solidification, which falls under kinetic fractionation [19]. The macrosegregation phenomenon of the mixture caused by non-equilibrium solidification also has the same mechanism. Macrosegregation refers to compositional inhomogeneities on a macroscopic scale [20]. Thus, in this simulation, a macrosegregation model was used to describe the occurrence of inhomogeneity. Numerical simulations were performed using ANSYS Fluent CFD software (Ansys, Inc.).

### 2.1. Assumptions

Macrosegregation models consider fundamental mechanisms involving heat transfer, species transport, fluid flow, solid movement, and phase equilibrium [21]. The main features and assumptions used to simplify the mathematical model are as follows.

- (1) The liquid phase of the hydrogen isotopologue mixture was an incompressible Newtonian fluid. The flow regime was assumed to be laminar.
- (2) The liquid and solid compositions could only be changed through diffusion.
- (3) The liquid and solid fractions were calculated using the lever rule.

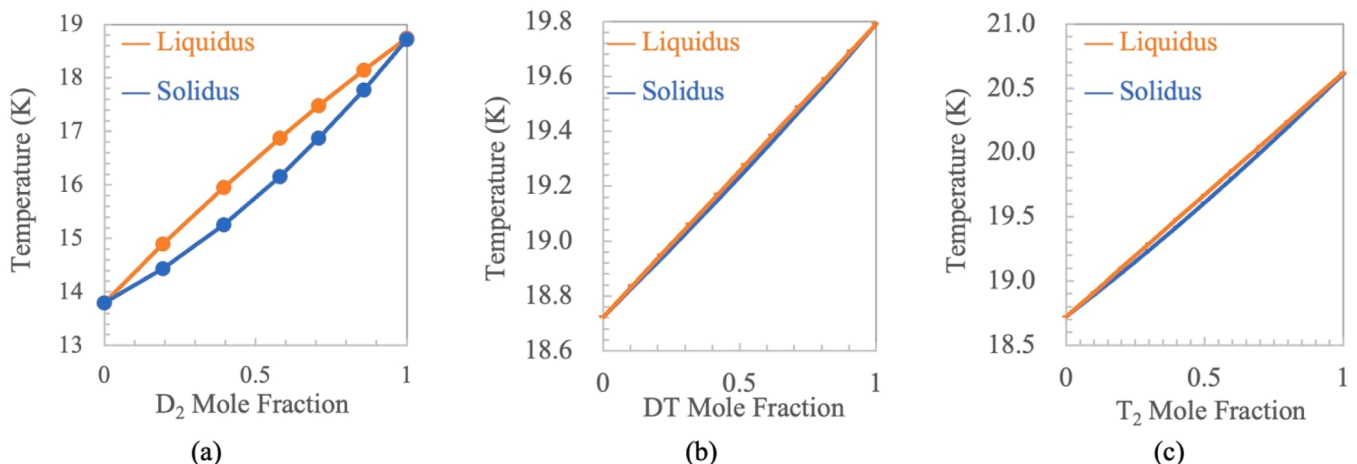


Fig. 3. Phase diagrams of (a)  $H_2$ - $D_2$ , (b)  $D_2$ -DT, and (c)  $D_2$ - $T_2$ .

- (4) The solid phase was considered stationary, and solidification shrinkage was not considered.
- (5) Except for density, the thermophysical properties of the liquid and solid phases were assumed to be the same and unchanged.
- (6) Negligible heat radiation exchange occurred with the surroundings.
- (7) The ortho–para conversion was negligible. The hydrogen was normal hydrogen (ortho–para ratio of 3:1), and the deuterium was normal deuterium (ortho–para ratio of 2:1) [16].

## 2.2. Phase equilibrium

Regarding the phase equilibrium, a linearized phase diagram was used to describe the relationship between the solute concentration of the phase and temperature during solidification. The H<sub>2</sub>-D<sub>2</sub> mixture was completely soluble. At cryogenic temperatures, although isotopic exchange will cause the H<sub>2</sub> and D<sub>2</sub> mixture to reach chemical equilibrium between H<sub>2</sub>, D<sub>2</sub>, and hydrogen deuteride (HD), the time required for the H<sub>2</sub>+D<sub>2</sub>⇌2HD exchange reaction to reach equilibrium is considerably longer than the duration of the experiment [16]; therefore, a catalyst must be added. The HD content at equilibrium is low [22]. Thus, the HD content was negligible in the simulation, and H<sub>2</sub> was used as the solvent in the simulation. The solidus and liquidus curves were fitted based on experimental data from the literature [17].

$$T_{\text{liquidus}} = 13.803 + 5.798 \times Y_{D_2} - 0.849 \times Y_{D_2}^2, \quad (1)$$

$$T_{\text{solidus}} = 13.803 + 2.896 \times Y_{D_2} + 2.021 \times Y_{D_2}^2, \quad (2)$$

where  $T_{\text{liquidus}}$  denotes the temperature of the liquidus,  $T_{\text{solidus}}$  denotes the temperature of the solidus,  $Y$  is the mole fraction. The standard deviations of the estimated  $T_{\text{liquidus}}$  and  $T_{\text{solidus}}$  values were 0.0304 and 0.0242, respectively. The phase diagram of H<sub>2</sub>-D<sub>2</sub> is shown in Fig. 3(a).

In contrast, for the D<sub>2</sub> and T<sub>2</sub> mixture, D<sub>2</sub>+T<sub>2</sub>⇌2DT exchange reaction can occur in hours or days. Meanwhile, the molecular vibrational zero-point of DT is higher than D<sub>2</sub> and T<sub>2</sub> [22]. Isotopologue molecules retain higher zero-point energy, leading to weaker intramolecular bonding. As the temperature approaches 0 K, DT molecules will increasingly convert into D<sub>2</sub> and T<sub>2</sub>. Therefore, for an initial 1:1 mixture of pure D<sub>2</sub> and T<sub>2</sub>, when the temperature drops to the freezing point, and equilibrium is reached, the ratio of D<sub>2</sub>, DT, and T<sub>2</sub> at equilibrium approaches 3:4:3[22]. Therefore, a ternary D<sub>2</sub>-DT-T<sub>2</sub> system was considered in the simulation. In FLUENT, only one component can be designated as a solute. In the ternary D<sub>2</sub>-DT-T<sub>2</sub> system, D<sub>2</sub> was designated as the solute, and the phase diagrams for D<sub>2</sub>-DT and D<sub>2</sub>-T<sub>2</sub> were plotted accordingly. Souers et al. [18] proposed a thermodynamic method to derive the solidus and liquidus curves of D<sub>2</sub>-DT-T<sub>2</sub> from the vapor pressure and vapor compositions. The solidus and liquidus curves were predicted using this method and the vapor pressure [22,23].

D<sub>2</sub>-DT:

$$T_{\text{liquidus}} = 18.723 + 1.067 \times Y_{DT}, \quad (3)$$

$$T_{\text{solidus}} = 18.723 + 0.978 \times Y_{DT} + 0.087 \times Y_{DT}^2. \quad (4)$$

D<sub>2</sub>-T<sub>2</sub>:

$$T_{\text{liquidus}} = 18.723 + 1.897 \times Y_{T_2}, \quad (5)$$

$$T_{\text{solidus}} = 18.723 + 1.649 \times Y_{T_2} + 0.024 \times Y_{T_2}^2. \quad (6)$$

Figs. 3(b) and 3(c) show the phase diagrams of D<sub>2</sub>-DT and D<sub>2</sub>-T<sub>2</sub>, respectively.

ANSYS Fluent was used to compute the solidus and liquidus temperatures in a species mixture, as follows [24]:

$$T_{\text{liquidus}} = T_{\text{melt}} + m_i Y_i, \quad (7)$$

**Table 1**

Slope of the liquidus and corresponding equilibrium partition coefficients.

	Slope of the Liquidus $m_i$	Partition Coefficient $K_i$
H <sub>2</sub> -D <sub>2</sub>	4.920	$10.928 - 1.055 \times T + 0.028 \times T^2$
D <sub>2</sub> -DT	.0671	$-1.304 + 0.315 \times T - 0.010 \times T^2$
D <sub>2</sub> -T <sub>2</sub>	1.897	$-1.754 + 0.349 \times T - 0.010 \times T^2$

$$T_{\text{solidus}} = T_{\text{melt}} + \frac{m_i Y_i}{K_i}, \quad (8)$$

where  $T_{\text{melt}}$  denotes the pure solvent melting temperature,  $Y_i$  is the mole fraction of the solute  $i$ ,  $m_i$  (a constant) is the slope of the liquidus with respect to  $Y_i$ , and  $K_i$  is the partition coefficient of solute  $i$ . The slope of the liquidus and corresponding equilibrium partition coefficients for each isotopologue composition are listed in Table 1.

## 2.3. Investigation of physical parameters

Behaviors, such as heat transfer and species transport, are affected by the physical properties of the components in the mixture. In Fluent, the physical properties of a mixed material and its constituent species must be defined. The thermodynamic properties of the species in the mixture are functions of temperature and can be defined using appropriate user-defined functions [24]. The temperature functions were defined using second-order polynomial regression equations. Based on the experimental values, we fitted the empirical regression equations using quadratic functions. Empirical formulas for density  $\rho_i$  (kg/m<sup>3</sup>) as a function of temperature  $T$  (K) of hydrogen isotopes are as follows:

H<sub>2</sub>:

$$\text{Liquid} : \rho_{H_2(l)} = 84.461 - 0.210 \times T - 0.022 \times T^2, \quad (9)$$

$$\text{Solid} : \rho_{H_2(s)} = 88.509 + 0.114 \times T - 0.019 \times T^2. \quad (10)$$

D<sub>2</sub>:

$$\text{Liquid} : \rho_{D_2(l)} = 207.560 - 1.468 \times T - 0.018 \times T^2, \quad (11)$$

$$\text{Solid} : \rho_{D_2(s)} = 204.100 - 0.221 \times T - 0.038 \times T^2. \quad (12)$$

T<sub>2</sub>:

$$\text{Liquid} : \rho_{T_2(l)} = 304.050 + 0.347 \times T - 0.089 \times T^2, \quad (13)$$

$$\text{Solid} : \rho_{T_2(s)} = 283.810 + 5.236 \times T - 0.191 \times T^2. \quad (14)$$

DT:

$$\text{Liquid} : \rho_{DT(l)} = 248.894 - 0.067 \times T^2, \quad (15)$$

$$\text{Solid} : \rho_{DT(s)} = 231.230 + 4.120 \times T - 0.154 \times T^2. \quad (16)$$

The experimental values of  $\rho_{H_2(l)}$ ,  $\rho_{D_2(l)}$ , and  $\rho_{T_2(l)}$  were obtained from Refs. [25–27]. The coefficients of determination ( $R_i^2$ ) for each regression equation were  $R_{H_2(l)}^2 \approx 1.0000$ ;  $R_{D_2(l)}^2 \approx 0.9996$ ;  $R_{T_2(l)}^2 \approx 0.9989$ . No experimental value for  $\rho_{H_2(s)}$ ,  $\rho_{D_2(s)}$ ,  $\rho_{T_2(s)}$ ,  $\rho_{DT(l)}$ , and  $\rho_{DT(s)}$  was found, and the empirical equations were obtained from the Refs. [28–30].

The empirical formulas of specific heat  $Cp_i$  (J/kg·K) as a function of temperature  $T$  (K) of hydrogen isotopes are as follows:

$$Cp_{H_2} = 411.850 + 375.810 \times T + 3.769 \times T^2, \quad (17)$$

$$Cp_{D_2} = 463.410 + 308.560 \times T - 2.303 \times T^2, \quad (18)$$

$$Cp_{T_2} = 3549.500 - 17.060 \times T + 0.663 \times T^2, \quad (19)$$

$$Cp_{DT} = 2006.455 + 145.750 \times T - 0.820 \times T^2. \quad (20)$$

The experimental values of  $Cp_{H_2}$  and  $Cp_{D_2}$  were obtained from Refs. [31] and [32]. The coefficients of determination for each regression equation were  $R^2_{Cp_{H_2}} \approx 0.9998$ ;  $R^2_{Cp_{D_2}} \approx 0.9944$ . The empirical equations for  $Cp_{T_2}$  were obtained from Ref. [33]. The  $Cp_{DT}$  was averaged from  $Cp_{D_2}$  and  $Cp_{T_2}$ . However, in an actual operational process, if  $Cp$  is set as a function, a floating-point exception occurs in the simulation. Therefore,  $Cp$  was set as a constant and calculated based on the initial temperature using Eqs. (17–20).

The empirical formulas of thermal conductivity  $K_i$  (W/m-K) as a function of temperature  $T$  (K) of hydrogen isotopes are as follows:

$$K_{H_2} = 0.0422 + 0.00457 \times T - 3.810 \times 10^{-5} \times T^2, \quad (21)$$

$$K_{D_2} = 0.0496 + 0.00524 \times T - 7.143 \times 10^{-5} \times T^2, \quad (22)$$

$$K_{T_2} = -0.0495 + 0.0134 \times T - 2.436 \times 10^{-4} \times T^2, \quad (23)$$

$$K_{DT} = 0.0222 + 0.0082 \times T - 1.458 \times 10^{-4} \times T^2. \quad (24)$$

The experimental values for  $K_{H_2}$ ,  $K_{D_2}$ , were obtained from Ref. [34]. The coefficients of determination for each regression equation were  $R^2_{K_{H_2}} \approx 0.9999$ ;  $R^2_{K_{D_2}} \approx 0.9860$ . The empirical equations for  $K_{DT}$  and  $K_{T_2}$  were obtained from Refs. [30] and [34], respectively.

The empirical formulas of viscosity  $\eta_i$  (kg/m-s) as a function of temperature  $T$  (K) of hydrogen isotopes are as follows:

$$\eta_{H_2} = 7.731 \times 10^{-5} - 5.023 \times 10^{-6} \times T + 9.256 \times 10^{-8} \times T^2, \quad (25)$$

$$\eta_{D_2} = 3.283 \times 10^{-4} - 2.475 \times 10^{-5} \times T + 5.098 \times 10^{-7} \times T^2, \quad (26)$$

$$\eta_{T_2} = 3.717 \times 10^{-4} - 2.231 \times 10^{-5} \times T + 3.608 \times 10^{-7} \times T^2, \quad (27)$$

$$\eta_{DT} = 2.751 \times 10^{-4} - 1.708 \times 10^{-5} \times T + 3.045 \times 10^{-7} \times T^2. \quad (28)$$

The experimental values of  $\eta_{H_2}$  and  $\eta_{D_2}$  were obtained from Refs. [35] and [29], respectively. The coefficients of determination for each regression equation were  $R^2_{\eta_{H_2}} \approx 1.0000$ ;  $R^2_{\eta_{D_2}} \approx 0.9958$ . The empirical equations for  $\eta_{T_2}$  and  $\eta_{DT}$  were obtained from Refs. [36] and [37], respectively.

Regarding the physical properties of the mixture material, the density, specific heat, thermal conductivity, and viscosity were set as mixing-law options, such that Fluent could be used to automatically calculate the value of the mixture based on that of each species. The mass-diffusion coefficient  $\mathfrak{D}_{D_2}$  ( $m^2/s$ ) of  $D_2$  in liquid  $H_2$ - $D_2$  was calculated using the following empirical formula [38]:

$$\mathfrak{D}_{D_2(l)} = 30.5e^{-36/T} \times 10^{-9}. \quad (29)$$

For the mass diffusion coefficients of liquid  $D_2$ - $T_2$  and  $D_2$ - $DT$ , no valid data or empirical formulas were found, and the Stokes-Einstein-Sutherland equation was used for the calculation.

$$\mathfrak{D}_i = \frac{k_B \cdot T}{6\pi \cdot \eta_j \cdot r_i}, \quad (30)$$

where  $k_B$  is the Boltzmann constant ( $1.38 \times 10^{-23}$  J/K),  $\eta_j$  is the dynamic viscosity of the medium, and  $r_i$  is the radius of the spherical particle. In the condensed state, the electron orbitals of hydrogen molecules have shapes that are closer to being spherical than dumbbell-shaped [39]. Hydrogen isotopes have the same molecular diameters [40] and shapes [41]. The diameter of the hydrogen molecule was 0.289 nm [42],  $r_{H_2} = r_{DT} = r_{T_2} = 1.445 \times 10^{-10}$  m. ANSYS Fluent was used to set the mass diffusion coefficient to a constant value. Based on the initial temperature, the viscosities are as in Eq. (26), after which the mass diffusion coefficient is calculated.

The interdiffusion coefficient  $\mathfrak{D}_{ij}$  in the solid phase was estimated using Darkan's equation [43].

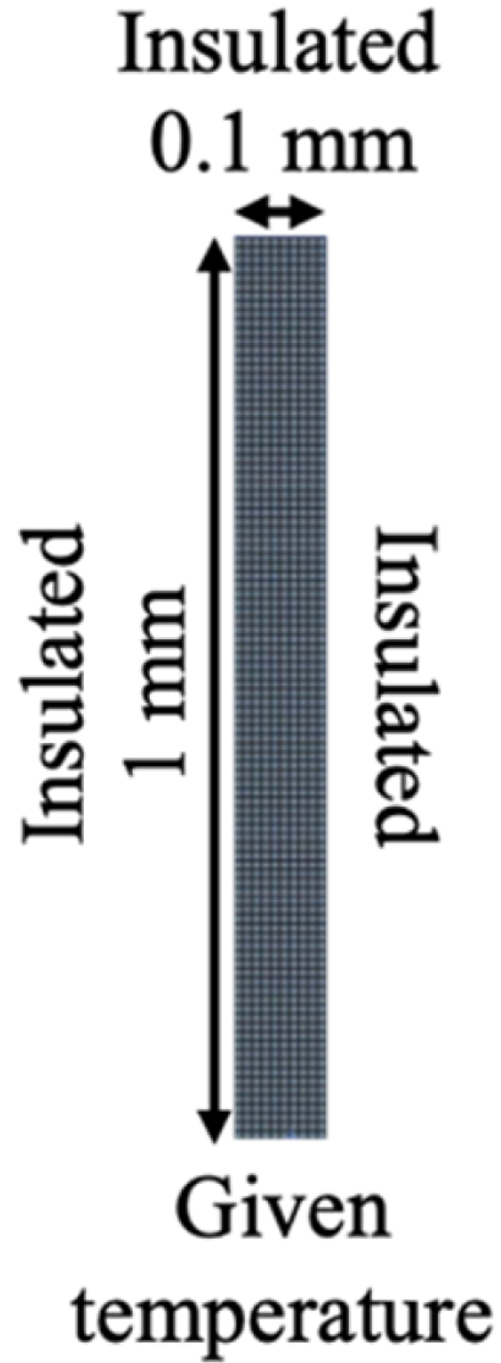


Fig. 4. Geometry and mesh to simulate solidification process the mixtures were solidified unidirectionally from the bottom.

$$\mathfrak{D}_{i-j} = \left( \mathfrak{D}_i^* Y_j + \mathfrak{D}_j^* Y_i \right), \quad (31)$$

where  $\mathfrak{D}_i^*$  is the intrinsic diffusion coefficient and  $Y_i$  is the mole fraction. The  $\mathfrak{D}_i^*$  can be expressed theoretically using the following equation:

$$\mathfrak{D}_i^* = \mathfrak{D}_i^0 \cdot e^{-\frac{E}{k_B T}}, \quad (32)$$

where  $\mathfrak{D}_i^0$  denotes the self-diffusion coefficient. The empirical equations for  $\mathfrak{D}_i^0$  are obtained from Ref. [44] and is expressed by the following equations:

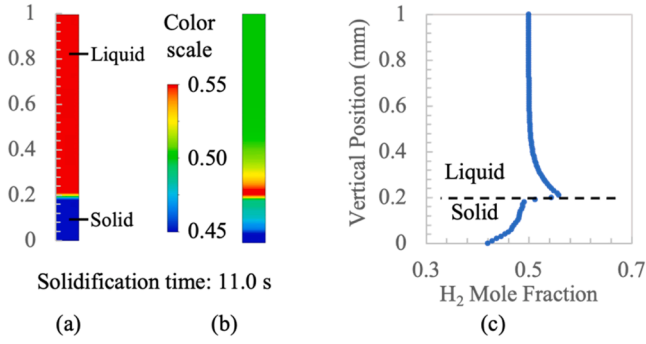


**Fig. 5.** (a) Liquid and solid-phase distribution. (b) Spatial distribution of H<sub>2</sub> mole fraction. (c) Vertical distribution of H<sub>2</sub> mole fraction.

$$\mathcal{D}_{H_2}^* = 2.8 \times 10^{-7} \times e^{-197/T}, \quad (33)$$

$$\mathcal{D}_{D_2}^* = 1.0 \times 10^{-6} \times e^{-300/T}, \quad (34)$$

$$\mathcal{D}_{DT}^* = 3.4 \times 10^{-5} \times e^{-372/T}, \quad (35)$$

$$\mathcal{D}_{T_2}^* = 1.8 \times 10^{-5} \times e^{-432/T}. \quad (36)$$

#### 2.4. Numerical solution procedure

When simulations were implemented, we selected the pressure-based solver to perform a transient calculation and simulate fluid flow, heat transfer, and species transport in the solidification process, enabling gravity and setting gravitational acceleration to  $-9.81 \text{ m/s}^2$  in the vertical direction. Considering the heat transfer, the conservation of energy equation was used to obtain the fluid temperature: the geometry and mesh were loaded, and all the necessary physical models, thermo-physical parameters, boundary conditions, and initial conditions were defined.

### 3. Results and discussion

#### 3.1. Factors affecting the homogeneity

Mass transport during solidification is responsible for macro-segregation. Mass transport through the diffusion of species results in diffusion-controlled macrosegregation [45]. Solidification rates significantly affect the distribution of solutes; the solidification process can be categorized into equilibrium and non-equilibrium solidification

processes. In equilibrium solidification, under infinitely slow solidification conditions, the solute completely diffuses in both the solid and liquid phases, ultimately forming a completely homogenized solid. Non-equilibrium solidification occurs when the solidification rate is so fast that diffusion is insufficient to homogenize the composition over time. There are two distinct conditions based on the diffusion of liquids: (1) no diffusion in solids and limited diffusion in liquids, and (2) no diffusion in solids and complete diffusion in liquids [46]. Both conditions result in the formation of inhomogeneous solids.

To clarify the mechanism of the compositional distribution change of hydrogen isotopologue mixtures during solidification and the effect of the solidification rate on homogeneity, the compositional distribution was simulated during the directional solidification of hydrogen isotopologue mixtures at different rates in a planar rectangle. The molar fraction ratio of H<sub>2</sub> to D<sub>2</sub> was 1:1. Initially, H<sub>2</sub> and D<sub>2</sub> were evenly dispersed in liquid. For simplification, a two-dimensional (2D) rectangular model of length 1 mm and width 0.1 mm was built. The mesh size was 0.01 mm, the mesh comprised 1000 elements, as shown in Fig. 4. The mixtures were solidified unidirectionally from the bottom along a long rectangular bar. The solidification rate was controlled by adjusting the bottom edge temperature. The heat was confined to the flow along the bar axis. Two limiting cases for the non-equilibrium solidification of H<sub>2</sub>-D<sub>2</sub> were simulated.

(I) No diffusion in solid; limited diffusion in liquid.

The initial temperature of liquid H<sub>2</sub>-D<sub>2</sub> was 16.5 K. The initial temperature of the bottom edge was set as 15.65 K. The total solidification time was 0.011 h. Liquid H<sub>2</sub>-D<sub>2</sub> solidified at a fast rate, with an average solidification rate of 90 mm/h; the average cooling rate was 175.5 K/h. Regarding the solidification process (I) in the initial stage of solidification (Fig. 5), the spatial distribution of the H<sub>2</sub> mole fraction is shown in Fig. 5(b). The average H<sub>2</sub> mole fraction in the horizontal direction of the sample was calculated to obtain the vertical gradient of the H<sub>2</sub> mole fraction (Fig. 5(c)). The D<sub>2</sub> triple point was higher and easier to solidify. D<sub>2</sub> rapidly accumulated in the formed solid; accordingly, H<sub>2</sub> remained in the liquid phase and rapidly accumulated ahead of the solid-liquid interface. This phenomenon is known as the initial transient phenomenon. The concentration distribution in the liquid should result in H<sub>2</sub> diffusing away from the interface along the concentration gradient. However, the H<sub>2</sub> in the liquid phase diffused insufficiently over time, and the H<sub>2</sub> content of the subsequently formed solid increased.

(II) When the diffusion rate was balanced by the rejection rate, the solidification reached a steady state (Fig. 6(a)). (III) As the solid/liquid interface approached the bar boundary, there was insufficient liquid ahead of the interface for H<sub>2</sub> to diffuse forward. The liquid phase was compressed to a very small volume, and the H<sub>2</sub> content at the interface increased rapidly, leading to a final transient, as shown in Fig. 6(b). (IV)

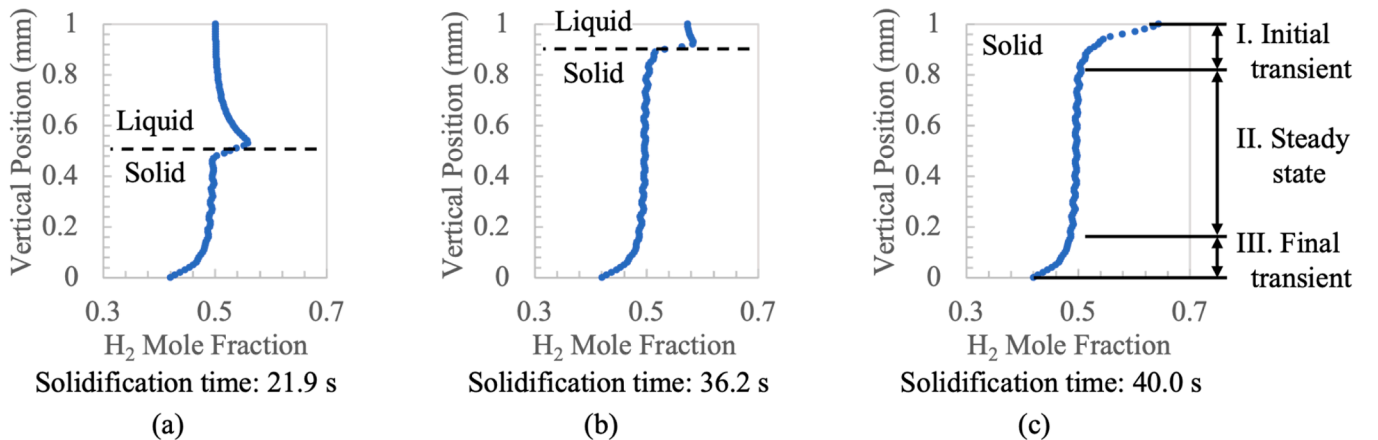


**Fig. 6.** (a) Vertical distribution of H<sub>2</sub> mole fraction at 21.9 s. (b) Vertical distribution of H<sub>2</sub> mole fraction at 36.2 s. (c) Vertical distribution of H<sub>2</sub> mole fraction at 40.0 s.

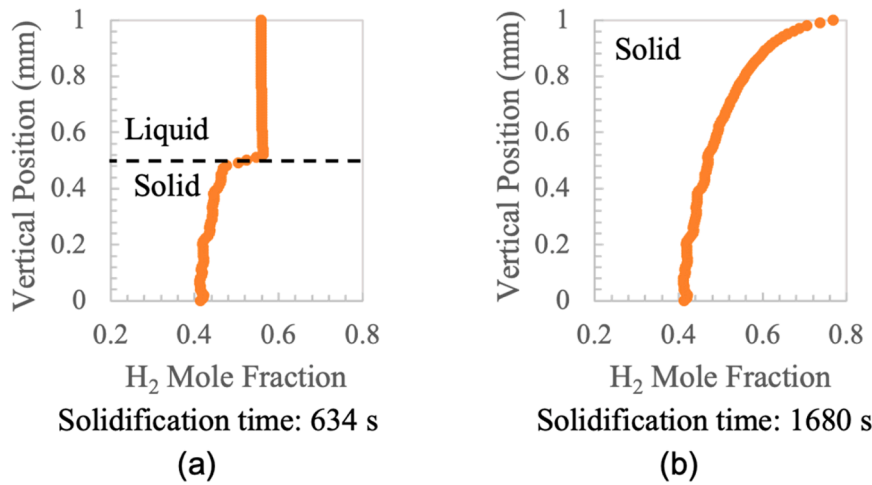


Fig. 7. (a) Vertical distribution of the H<sub>2</sub> mole fraction at 634 s. (b) Vertical distribution of the H<sub>2</sub> mole fraction at 1680 s.

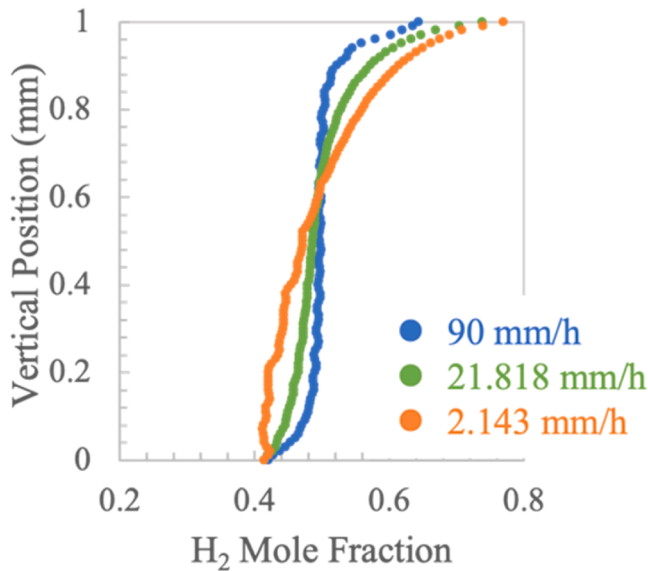


Fig. 8. Comparison of H<sub>2</sub> molar fractions of H<sub>2</sub>-D<sub>2</sub> solidified at different rates.

After 40 s, the liquid H<sub>2</sub>-D<sub>2</sub> mixture completely solidified. As the rate of diffusion in the solid was negligible, the molar fraction gradient formed at each stage was maintained, leading to an obvious macrosegregation phenomenon in the H<sub>2</sub>-D<sub>2</sub> solid (Fig. 6(c)). In this study, the segregation differences were used to evaluate the degree of segregation. The segregation difference is described as follows [47]:

$$\Delta A = \frac{C_{max} - C_{min}}{C_0} \times 100\%, \quad (37)$$

where  $C_0$  is the initial H<sub>2</sub> content and  $C_{max}$  and  $C_{min}$  are the highest and lowest H<sub>2</sub> contents of the sample, respectively. The segregation difference of solid H<sub>2</sub>-D<sub>2</sub> was 44.771 %.

(2) No diffusion in solids; complete diffusion in liquids.

The initial temperature of liquid H<sub>2</sub>-D<sub>2</sub> was 16.5 K. The initial temperature of the bottom edge was set as 15.65 K. The total solidification time was 0.467 h. H<sub>2</sub>-D<sub>2</sub> solidified at a relatively low rate, with an average solidification rate of 2.143 mm/h and average cooling rate of 1.607 K/h. After H<sub>2</sub> was excluded from the solid phase and remained in the liquid, sufficient diffusion occurred, resulting in an approximately homogeneous liquid phase, and the H<sub>2</sub> content in the final solid increased gradually (Fig. 7(a)). In the final stage of solidification, the H<sub>2</sub>

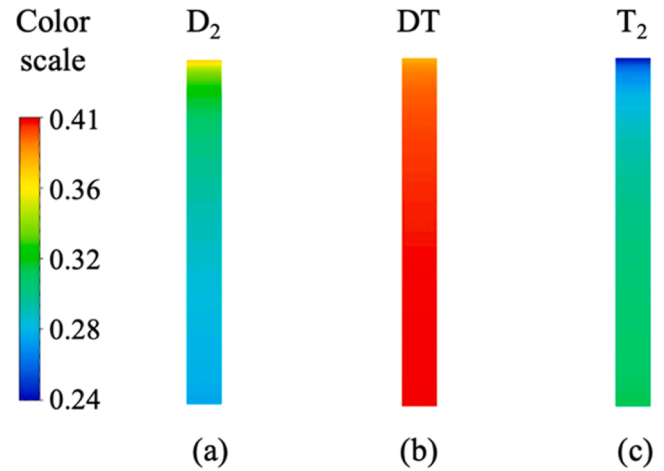


Fig. 9. (a) Spatial distribution of D<sub>2</sub> mole fraction. (b) Spatial distribution of DT mole fraction. (c) Spatial distribution of T<sub>2</sub> mole fraction.

content in the remaining liquid was higher and the inhomogeneity of the final solid increased (Fig. 7(b)). The segregation difference of solid H<sub>2</sub>-D<sub>2</sub> was 70.928 % according to Eq. (37).

Fig. 8 compares the H<sub>2</sub> mole fractions of H<sub>2</sub>-D<sub>2</sub> solidified at different rates, indicating that when solid diffusion is negligible, the separation degree of the final solid is related to diffusion in the liquid phase. As the solidification rate was slow enough to allow sufficient time for diffusion in the liquid, the segregation difference approached its maximum value.

The macrosegregation of D<sub>2</sub>-T<sub>2</sub> and D<sub>2</sub>-DT-T<sub>2</sub> was also simulated. The fusion reaction requires D<sub>2</sub>, DT, and T<sub>2</sub> molecules to reach the plasma state; the homogeneity of the fuel target is indicated by the distribution of D atoms. In the D<sub>2</sub>-T<sub>2</sub> mixture, only two molecules, D<sub>2</sub> and T<sub>2</sub> are present, and the mole fraction of D<sub>2</sub> molecules were equal to that of D atoms. The initial molar fraction of T<sub>2</sub> was 0.5, the initial temperature of liquid D<sub>2</sub>-T<sub>2</sub> was 19.7 K, and the initial temperature of the bottom edge was set to 19.56 K. The total solidification time, average solidification rate, and average cooling rate were 0.318 h, 3.144 mm/h, and 1.258 K/h, respectively.

Regarding the D<sub>2</sub>-DT-T<sub>2</sub> mixture, the initial molar fraction of DT and T<sub>2</sub> were 0.4 and 0.3, respectively; initial temperature of the liquid D<sub>2</sub>-T<sub>2</sub> was 19.72 K; and initial temperature of the bottom edge was set to 19.62 K. The total solidification time, average solidification rate, and average cooling rate were 0.304 h, 3.285 mm/h, and 0.821 K/h, respectively. The mole fraction profile of each molecule in the solid phase is shown in

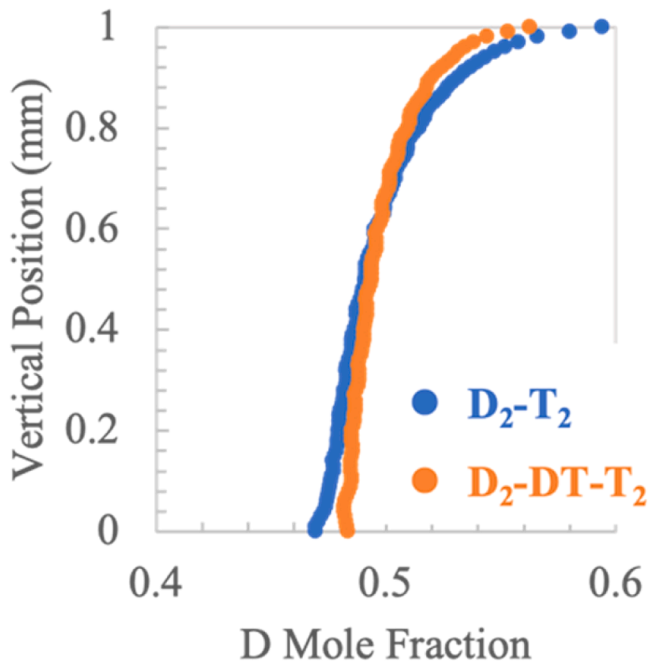


Fig. 10. Comparison of mole fractions of D atoms in  $D_2-T_2$  and  $D_2-DT-T_2$ .

Fig. 9. The molar fractions of D atoms ( $Y_D$ ) are calculated as follows:

$$Y_D = 1 \times Y_{D_2} + 0.5 \times Y_{DT} + 0 \times Y_{T_2}. \quad (38)$$

Fig. 10 shows the vertical distribution of D atoms in solid  $D_2-T_2$  and  $D_2-DT-T_2$  formed when there was no solid diffusion and the liquid was fully diffused. From Eq. (37), the maximum segregation difference of  $D_2-T_2$  and  $D_2-DT-T_2$  are approximately 24.980 % and 16.351 %, respectively. Ideally, D atoms should be distributed in the solid D-T fuel layer with a molar fraction as close as possible to 0.5. The maximum segregation difference close to 0 indicates that the degree of homogeneity is higher. The comparison shows that the amplitude of the D molar fraction in  $D_2-DT-T_2$  is smaller and more homogeneous.  $D_2-DT-T_2$  can form higher quality solid D-T fuel layer. Constructing a simulation method to quantify the effect of the degree of homogeneity on fusion reactions will be a future work.

Therefore, according to the mechanism of component distribution change during solidification and the factors affecting homogeneity, the following methods were considered for homogenizing the solid D-T fuel layer:

- (1) Solidification should be performed as quickly as possible. However, in the actual experiments, the solidification rate was excessively high, leading to the formation of dendrites. Gaps are easily formed between the dendrites, resulting in a loose solid structure. Therefore, based on avoiding dendritic crystallization, rapid solidification can improve the homogeneity of the solid D-T fuel layer.
- (2) Solidification should be maintained at an extremely slow rate. In addition to the liquid phase, the solid-phase components must diffuse as efficiently as possible throughout the solidification process. When the solidification process is infinitely close to equilibrium solidification, the solid D-T fuel layer is infinitely close to being homogeneous. Therefore, it is practically impossible to remedy or remove macrosegregation by heat treatment, because species can only move over distances on a microscopic scale [48].
- (3) Owing to the presence of the DT molecules,  $D_2-DT-T_2$  formed a more homogeneous solid D-T fuel layer. The high temperature strips the electrons from the atoms to form plasma [49]; the solid

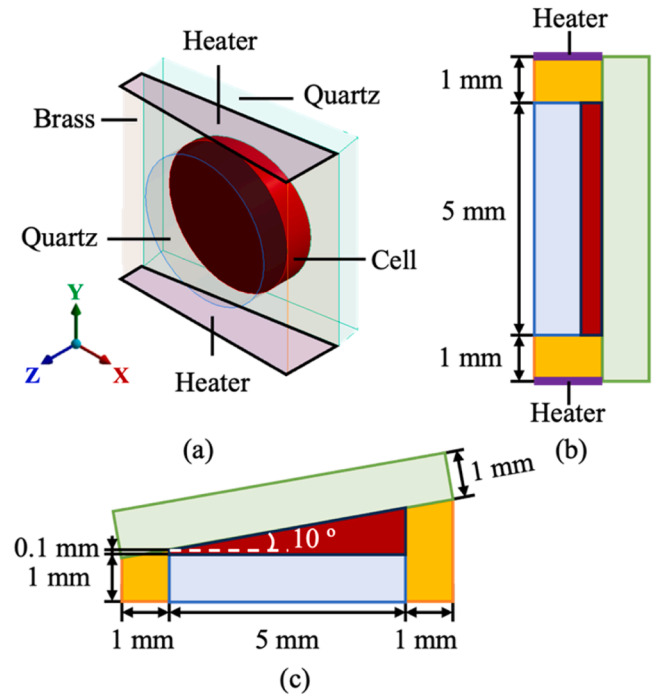


Fig. 11. (a) 3-dimensional structure of the cell. (b) Cross-section of the middle of the cell in the x direction. (c) Cross-section of the middle of the cell in the y direction.

D-T fuel layer only requires a uniform distribution of D and T atoms. Therefore,  $D_2$  and  $T_2$  can be mixed and left to stand for an extended period, such that the isotope exchange reaches an equilibrium state, thereby obtaining the maximum DT content. Subsequently,  $D_2-DT-T_2$  can be used to create a solid D-T fuel layer.

- (4) Vibration or stirring during solidification facilitates homogenization. Fluid flow can refine the grain size and homogenize the distribution of molecules in the solid D-T fuel layer. For example, it has been reported that ultrasonic vibration can refine the grain size and homogenize the distribution of nanoparticles in the melt [50].

### 3.2. Homogeneity of 3D hydrogen isotopologue mixture samples during the solidification process

#### 3.2.1. Geometry and boundary conditions

In the refractive-index distribution measurement experiment, a wedge cavity composed of brass and quartz glass was used to fill the hydrogen isotopologue mixture. Details of the cell structure are described in our previous study [51]. Initially, the bottom temperature was set slightly below the solidification temperature of hydrogen isotopologue mixtures, and the top temperature was set slightly above the solidification temperature. Reducing the temperature controlled the crystals to grow slowly from the bottom of the cell, avoiding gaps formed due to solidification shrinkage. The cell geometry was modeled three-dimensionally using Fluent (Fig. 11). The main focus of our study was the solidification behavior of the liquid in the cell; therefore, the inlet and outlet were not considered, and the simulation began when the liquid entirely filled the cell. The cell area was directly set as the hydrogen isotope mixture.

Performing simulations with ANSYS Fluent requires meshing a continuous geometric space to discretize and analyze the simulation. The computation was performed using a structured mesh comprising 449,883 elements, which were refined from the cell. The mesh size was 0.1 mm.

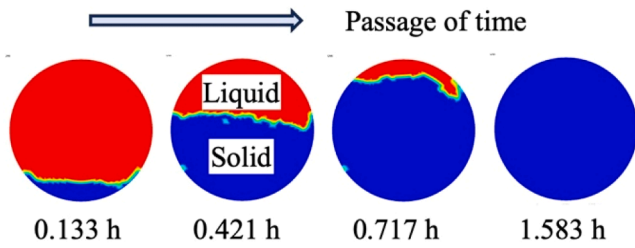


Fig. 12. Solidification process of H<sub>2</sub>-D<sub>2</sub>.

In this experiment, the cells were placed in a vacuum cryostat. To control the cell temperature, heaters and temperature sensors were attached at the top and bottom of the cell. The boundary conditions considered applicable to the cell are as follows: (1) Uniform temperatures were applied to the top and bottom surfaces of the brass cell. (2) The wall surface was set as adiabatic. (3) Only heat conduction between the surfaces of objects in contact with each other was considered.

3.2.2. Homogeneity of H<sub>2</sub>-D<sub>2</sub> 3D sample during solidification process

In 2021, a wedge-shaped sample of the H<sub>2</sub>-D<sub>2</sub> mixture was solidified in a well-controlled experiment (with the temperature difference between the two ends maintained about 0.4 K) [16]. In this study, the simulation model was expanded from a 2D plane to a three-dimensional (3D) solid model. The initial conditions for the simulation of H<sub>2</sub>-D<sub>2</sub> mixtures were set according to the experimental conditions. D<sub>2</sub>, with a molar fraction of 0.5, was evenly dispersed in the liquid. The initial temperature of liquid H<sub>2</sub>-D<sub>2</sub> was 16.200 K, and the initial temperatures of the top and bottom surfaces of brass were set to 16.138 K and 15.651 K, respectively. The temperatures were reduced in stages at the same

time intervals as those used in the experiment. The total solidification time was 1.583 h, average solidification rate was 3.158 mm/h, and average cooling rates at the top and bottom were 0.531 and 0.397 K/h, respectively. Fig. 12 shows the solidification process for H<sub>2</sub>-D<sub>2</sub>.

In the refractive-index measurement experiment, a vertical line laser was incident perpendicular to the center of the H<sub>2</sub>-D<sub>2</sub> cell, and the vertical distribution of the H<sub>2</sub> mole fraction was calculated using the refractive-index distribution. Fig. 13(a) shows the cell observation window. The simulation also analyzed the H<sub>2</sub> mole fraction distribution in the cross-section at the center of the cell (Fig. 13(b)). Fig. 13(c) shows the distribution of the liquid and solid phases in the cross-section, and Fig. 13(d) shows the distribution of the corresponding H<sub>2</sub> mole fractions. Fig. 13(e) shows the vertical distribution of the average H<sub>2</sub> mole fraction in the horizontal direction of the cell compared with the experimental values. A reasonable agreement was obtained between the calculated results and the experimentally measured H<sub>2</sub> mole fractions.

The experimental data were discontinuous around the solid-liquid interface. The previously analyzed reason was that because the interface was not horizontal, the path of the incident laser was altered by refraction or scattering as it passed through the interface, leading to partial data loss. This was well demonstrated by the simulation results; as the temperature decreased, liquid crystallized easily on the glass window surface due to the thermal conductivity of the glass, resulting in a non-horizontal interface (Fig. 14(b)). In addition, Fig. 11(b) shows that the heater was on the right side of the cell; therefore, the right side of H<sub>2</sub>-D<sub>2</sub> solidified more rapidly.

The densities of H<sub>2</sub>-D<sub>2</sub> are higher in the solid state than in the liquid state; therefore, during the solidification process, the volume of H<sub>2</sub>-D<sub>2</sub> undergoes contraction, which results in the formation of defects, such as shrinkage cavities, voids, shrink marks, and micropores (Fig. 15(a)). Shrinkage cavities began to appear at a later stage because of the

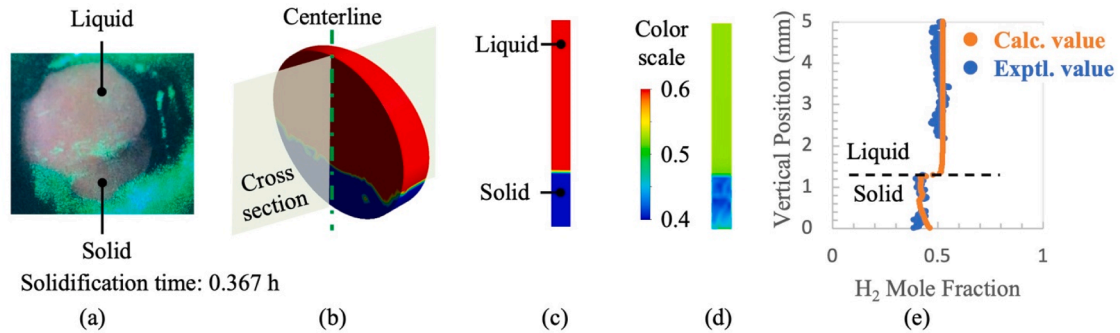


Fig. 13. (a) Observation window of cell. (b) Schematic of cross-section location. (c) Liquid and solid-phase distribution in cross-section. (d) Spatial distribution of H<sub>2</sub> mole fraction in cross-section. (e) Comparison of calculated and experimental values.

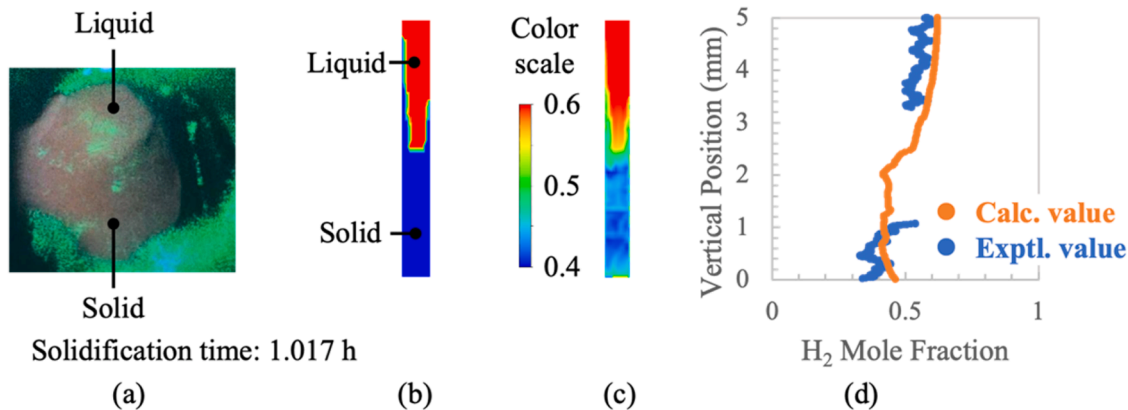
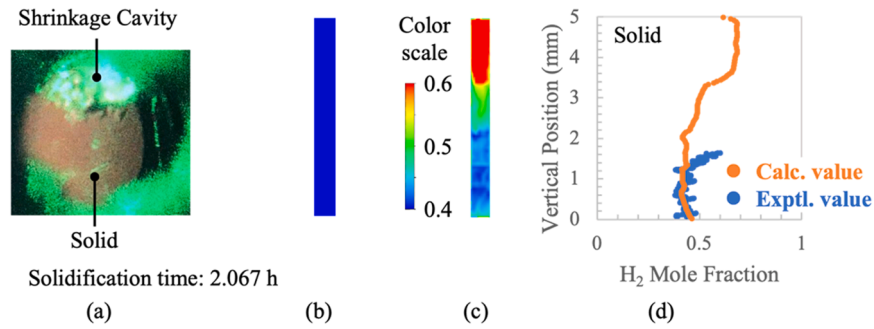
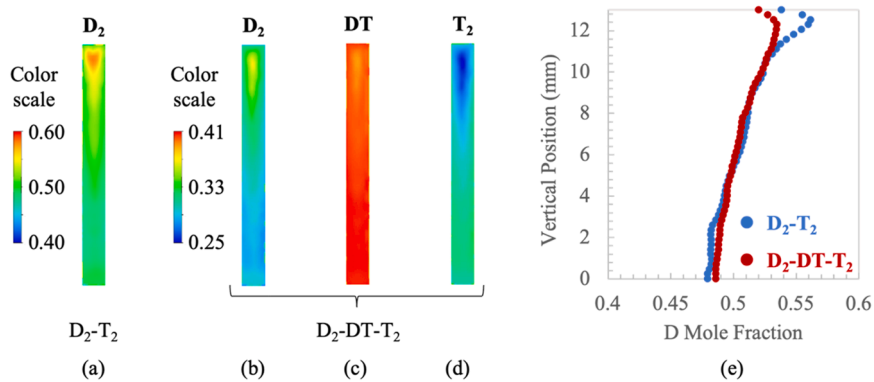


Fig. 14. (a) Observation window of cell. (b) Liquid and solid-phase distribution in cross-section. (c) Spatial distribution of H<sub>2</sub> mole fraction in cross-section. (d) Comparison of calculated and experimental values.



**Fig. 15.** (a) Observation window of cell. (b) Liquid and solid-phase distribution in cross-section. (c) Spatial distribution of H<sub>2</sub> mole fraction in cross-section. (d) Comparison of calculated and experimental values.



**Fig. 16.** (a) Spatial distribution of D<sub>2</sub> mole fraction in D<sub>2</sub>-T<sub>2</sub>. (b) Spatial distribution of D<sub>2</sub> mole fraction in D<sub>2</sub>-DT-T<sub>2</sub>. (c) Spatial distribution of DT mole fraction in D<sub>2</sub>-DT-T<sub>2</sub>. (d) Spatial distribution of T<sub>2</sub> mole fraction in D<sub>2</sub>-DT-T<sub>2</sub>. (e) Comparison of mole fractions of D atoms in D<sub>2</sub>-T<sub>2</sub> and D<sub>2</sub>-DT-T<sub>2</sub>.

residual H<sub>2</sub>-D<sub>2</sub> in the filling pipe, and the contraction of volume became apparent once the solid H<sub>2</sub>-D<sub>2</sub> blocked the pipe. The simulation of shrinkage cavity formations requires more complex numerical modeling; the current simulation has some limitations in simulating this; however, it will be addressed in future work. According to Eq. (37), the segregation differences of solid H<sub>2</sub>-D<sub>2</sub> in the experimental and calculated data are approximately 43.393 % and 54.814 %, respectively. The segregation difference of the calculated data is larger than that in the experimental data because the experimental data for the upper part of the cell, where H content is higher are missing.

### 3.2.3. Homogeneity of D<sub>2</sub>-T<sub>2</sub> and D<sub>2</sub>-DT-T<sub>2</sub> 3D samples during the solidification process

At present, we have not yet obtained the results of measurement experiments on the homogeneity of the D<sub>2</sub>-T<sub>2</sub> and D<sub>2</sub>-DT-T<sub>2</sub> cells; however, simulations of the distribution of D atoms in the cross-section of the cell have been performed. Regarding the initial conditions of the D<sub>2</sub>-T<sub>2</sub> mixture, the molar fraction of T<sub>2</sub> was 0.5, initial temperature of liquid D<sub>2</sub>-T<sub>2</sub> was 19.75 K, and initial temperatures of the top and bottom were set to 19.75 K and 19.5 K, respectively. The total solidification time was 0.45 h, the average solidification rate was 11.111 mm/h, and the average cooling rates of the top and bottom were 0.556 and 0.444 K/h, respectively. Fig. 16(a) shows the distribution of the D<sub>2</sub> mole fraction of solid D<sub>2</sub>-T<sub>2</sub>.

Regarding the initial conditions of the D<sub>2</sub>-DT-T<sub>2</sub> mixture, the molar fractions of DT and T<sub>2</sub> were 0.4 and 0.3, respectively; initial temperature of liquid D<sub>2</sub>-DT-T<sub>2</sub> was 19.80 K; and initial temperatures of top and bottom were set to 19.8 K and 19.55 K, respectively. The total solidification time was 0.45 h, average solidification rate was 11.111 mm/h, and average cooling rates of the top and bottom layers were 0.667 and 0.533 K/h, respectively. Figs. 16(b), (c), and (d) show the mole fraction profiles of each molecule in the solid D<sub>2</sub>-DT-T<sub>2</sub>. The molar fractions of

the D atoms were calculated using Eq. (38). Fig. 16(e) shows the vertical distribution of D atoms in solid D<sub>2</sub>-T<sub>2</sub> and D<sub>2</sub>-DT-T<sub>2</sub>. The solid D<sub>2</sub>-DT-T<sub>2</sub> was more homogeneous. We will characterize the homogeneity of the D<sub>2</sub>-T<sub>2</sub> and D<sub>2</sub>-DT-T<sub>2</sub> mixtures by refractive index measurement experiments in future work. These simulation results can be used to predict future experimental results, which can in turn verify the simulation results.

The effect of the decay heat of tritium on solidification was also simulated; however, the results indicated that the decay heat effect was not significant during solidification.

## 4. Conclusion

Inhomogeneity is a major defect in the solid D-T layer that affects the final performance of the fuel target. This study demonstrated a method for numerically simulating the homogeneity of solid hydrogen isotope mixtures using a macrosegregation model. The fluid flow, heat, and species transport during the solidification of hydrogen isotopologue mixtures were simulated and analyzed. First, the non-equilibrium solidification process of hydrogen isotopologue mixtures was simulated in a 2D plane, and the mechanism of the composition distribution change and effect of the solidification rate on homogeneity were elucidated. Under non-equilibrium solidification conditions, when the contribution of diffusion to changes in the composition of the solid was negligible, the solidification rate was faster, leading to higher homogeneity in the final solid. Furthermore, D<sub>2</sub>-DT-T<sub>2</sub> formed a more homogeneous solid than D<sub>2</sub>-T<sub>2</sub>. Therefore, it is considered to improve the homogeneity of the solid D-T fuel layer by controlling the solidification rate and increasing the DT molecular content. Improved homogeneity is important for the fabrication of high-quality D-T fuel pellets.

Meanwhile, in this study, the homogeneity of hydrogen isotope mixtures was simulated using a 3D model. Reasonable agreement was

achieved between the calculated and experimental results for H<sub>2</sub>-D<sub>2</sub>; the differences were satisfactorily explained, demonstrating the validity of the simulation method. Subsequently, the homogeneities of D<sub>2</sub>-T<sub>2</sub> and D<sub>2</sub>-DT-T<sub>2</sub> were simulated using this method, which can be verified through future experimental measurements. This study explored the factors affecting the homogeneity of hydrogen isotopologue mixtures during solidification and demonstrated a simulation method for predicting the homogeneity of solid D-T layer in the fuel pellets. Based on the factors affecting the homogeneity, possible methods to improve the homogeneity are given; these methods will be further demonstrated for feasibility in future work. We expected this study will contribute to improving the quality of D-T fuel pellets. stigation

### CRediT authorship contribution statement

**Jiaqi Zhang:** Writing – original draft, Visualization, Software, Methodology, Investigation, Formal analysis, Data curation, Conceptualization. **Akifumi Iwamoto:** Writing – review & editing, Supervision, Project administration, Methodology, Formal analysis. **Keisuke Shigemori:** Writing – review & editing, Supervision, Project administration. **Masanori Hara:** Writing – review & editing, Validation, Supervision, Investigation, Conceptualization. **Kohei Yamanoi:** Writing – review & editing, Supervision, Project administration, Methodology, Funding acquisition, Conceptualization.

### Declaration of competing interest

The authors declare that they have no known competing financial interests or personal relationships that could have appeared to influence the work reported in this paper.

### Acknowledgment

The authors acknowledge the support of the Institute of Laser Engineering at Osaka University and the National Institute for Fusion Science and the Hydrogen Isotope Research Centre, Toyama University, and Osaka University Fellowship “Quantum Leader Resources” for their support of this work. This study was supported by the QST Research Collaboration for Fusion DEMO and JSPS KAKENHI (grant number: 22H01204).

### Data availability

No data was used for the research described in the article.

### References

- T.C. Sangster, R. Betti, R.S. Craxton, J.A. Delettrez, D.H. Edgell, et al., Cryogenic DT and D<sub>2</sub> targets for inertial confinement fusion, *Phys. Plasmas* 14 (5) (2007) 058101, <https://doi.org/10.1063/1.2671844>.
- R. Epstein, S.P. Regan, B.A. Hammel, L.J. Suter, H.A. Scott, et al., Applications and results of X-ray spectroscopy in implosion experiments on the National Ignition Facility, *AIP Conf. Proc.* 1811 (1) (2017) 190004, <https://doi.org/10.1063/1.4975747>.
- J.L. Kline, S.H. Batha, L.R. Benedetti, D. Bennett, S. Bhandarkar, Progress of indirect drive inertial confinement fusion in the United States, *Nucl. Fusion* 59 (11) (2019) 112018, <https://doi.org/10.1088/1741-4326/ab1ecf>.
- Z. Li, Z.Q. Zhao, X.H. Yang, G.B. Zhang, Y.Y. Ma, et al., Hybrid optimization of laser-driven fusion targets and laser profiles, *Plasma Phys. Control. Fusion* 66 (1) (2024) 015010, <https://doi.org/10.1088/1361-6587/ad0e21>.
- D.L. Musinski, T.M. Henderson, R.J. Simms, T.R. Pattinson, R.B. Jacobs, et al., Technological aspects of cryogenic laser-fusion targets, *J. Appl. Phys.* 51 (3) (1980) 1394–1402, <https://doi.org/10.1063/1.327836>.
- J. Nuckolls, L. Wood, A. Thiessen, G. Zimmerman, Laser compression of matter to super-high densities: thermonuclear (CTR) applications, *Nature* 239 (5368) (1972) 139–142, <https://doi.org/10.1038/239139a0>.
- S. Kawata, K. Niu, Effect of nonuniform implosion of target on fusion parameters, *JPSJ* 53 (10) (1984) 3416–3426, <https://doi.org/10.1143/JPSJ.53.3416>.
- H. Takeda, K. Niu, Numerical analysis for effects of irradiation nonuniformities on target implosion. I. 2-dimensional simulation, *JPSJ* 57 (6) (1988) 1987–1999, <https://doi.org/10.1143/JPSJ.57.1987>.
- R.L. McCrory, R.E. Bahr, R. Betti, T.R. Boehly, T.J.B. Collins, et al., OMEGA ICF experiments and preparation for direct drive ignition on NIF, *Nucl. Fusion* 41 (10) (2001) 1413, <https://doi.org/10.1088/0029-5515/41/10/309>.
- C. Kendall, E.A. Caldwell, Fundamentals of isotope geochemistry, in: C. Kendall, J. J. McDonnell (Eds.), *Isotope Tracers in Catchment Hydrology*, Elsevier Science B. V., Amsterdam, 1998, pp. 51–86, <https://doi.org/10.1016/B978-0-444-81546-0.50009-4>.
- J.K. Hofer, L.R. Foreman, Radioactively induced sublimation in solid tritium, *Phys. Rev. Lett.* 60 (13) (1988) 1310, <https://doi.org/10.1103/PhysRevLett.60.1310>.
- D.N. Bittner, G.W. Collins, E. Monsler, S. Letts, Forming uniform HD layers in shells using infrared radiation, *Fusion Technol.* 35 (2) (1999) 244–249, <https://doi.org/10.13182/FST99-A11963931>.
- D.R. Harding, M.D. Wittman, D.H. Edgell, Considerations and requirements for providing cryogenic targets for direct-drive inertial fusion implosions at the National Ignition Facility, *Fusion Sci. Technol.* 63 (2) (2012) 95–105, <https://doi.org/10.13182/FST13-A16326>.
- K. Iwano, A. Iwamoto, K. Yamanoi, Y. Arikawa, H. Nagatomo, et al., Preliminary cryogenic layering by the infrared heating method modified with cone temperature control for the polystyrene shell FIREX target, *Plasma Fusion Res.* 16 (2021) 1404099, <https://doi.org/10.1585/pfr.16.1404099>.
- A. Iwamoto, T. Fujimura, T. Norimatsu, Void free fuel solidification in a foam shell FIREX target, *Plasma Fusion Res.* 15 (2020) 2404006, <https://doi.org/10.1585/pfr.15.2404006>.
- J. Zhang, A. Iwamoto, K. Shigemori, M. Hara, K. Yamanoi, Refractive index measurement of hydrogen isotopologue mixture and applicability for homogeneity of hydrogen solid at cryogenic temperature in fusion fuel system, *Nucl. Fusion* 63 (7) (2023) 076020, <https://doi.org/10.1088/1741-4326/acd015>.
- D. White, J.R. Gaines, Liquid–solid phase equilibria in the hydrogen–deuterium system, *J. Chem. Phys.* 42 (12) (1965) 4152–4158, <https://doi.org/10.1063/1.1695911>.
- P.C. Souers, R.G. Hickman, R.T. Tsugawa, Estimated D<sub>2</sub>-DT-T<sub>2</sub> Phase Diagram in the Three-Phase Region, Lawrence Livermore Lab., California Univ., Livermore (USA), 1975.
- J. Zhang, A. Iwamoto, K. Shigemori, M. Hara, K. Yamanoi, Refractive index measurements of solid hydrogen isotopologues, *Fusion Sci. Technol.* 80 (3–4) (2024) 550–557, <https://doi.org/10.1080/15361055.2023.2197810>.
- A. Ludwig, W. Wu, A. Kharicha, On macrosegregation, *Metall. Mater. Trans. A* 46 (2015) 4854–4867, <https://doi.org/10.1007/s11661-015-2959-4>.
- C. Beckermann, Modelling of macrosegregation: applications and future needs, *Int. Mater. Rev.* 47 (5) (2002) 243–261, <https://doi.org/10.1179/095066002225006557>.
- P.C. Souers, Cryogenic Hydrogen Data Pertinent to Magnetic Fusion Energy, Lawrence Livermore Lab., California Univ., Livermore (USA), 1979, <https://doi.org/10.2172/6205719>.
- J. Noh, A.M. Fulguras, L.J. Sebastian, H.G. Lee, D.S. Kim, et al., Estimation of thermodynamic properties of hydrogen isotopes and modeling of hydrogen isotope systems using Aspen Plus simulator, *J. Ind. Eng. Chem.* 46 (2017) 1–8, <https://doi.org/10.1016/j.jiec.2016.07.053>.
- U.D.F. Manual, ANSYS FLUENT 12.0. Theory guide, (2009).
- R.D. Goodwin, D.E. Diller, H.M. Roder, L.A. Weber, The densities of saturated liquid hydrogen, *Cryogenics* 2 (2) (1961) 81–83, [https://doi.org/10.1016/0011-2275\(61\)90025-X](https://doi.org/10.1016/0011-2275(61)90025-X).
- J.E. Jensen, R.B. Stewart, W.A. Tuttle, H. Brechna, A.G. Prodel, Properties of deuterium. Brookhaven National Laboratory Selected Cryogenic Data Notebook, Brookhaven National Laboratory, Associated Universities, Incorporated, 1980, p. 136.
- E.R. Grilly, The densities of liquid tritium, 20.6 to 29° K, *J. Am. Chem. Soc.* 73 (11) (1951) 5307–5308, <https://doi.org/10.1021/ja01155a089>.
- G. Ahlers, Some Properties of Solid Hydrogen At Small Molar Volumes, Lawrence Radiation Lab, California Univ., Livermore (USA), 1963, p. 86.
- H.M. Roder, G.E. Childs, R.D. McCarty, P.E. Angerhofer, Survey of the Properties of the Hydrogen Isotopes Below Their Critical Temperatures, U.S. Government Printing Office, 1973, p. 14, <https://doi.org/10.2172/4244810>.
- P.W. Fisher, Tritium Proof-of-Principle Pellet Injector, Oak Ridge National Lab., TN (United States), 1991, pp. 42–43, <https://doi.org/10.2172/5182817>.
- B.A. Younglove, D.E. Diller, The specific heat of saturated liquid para-hydrogen from 15 to 32° K, *Cryogenics* 2 (5) (1962) 283–287, [https://doi.org/10.1016/0011-2275\(62\)90011-5](https://doi.org/10.1016/0011-2275(62)90011-5).
- E.C. Kerr, E.B. Rifkin, H.L. Johnston, J.T. Clarke, Condensed gas calorimetry. II. Heat capacity of ortho-deuterium between 13.1 and 23.6° K., melting and boiling points, heats of fusion and vaporization, vapor pressures of liquid ortho-deuterium, *J. Am. Chem. Soc.* 73 (1) (1951) 282–284, <https://doi.org/10.1021/ja01145a093>.
- W.M. Jones, Thermodynamic functions for tritium and tritium hydride. The equilibrium of tritium and hydrogen with tritium hydride. The dissociation of tritium and tritium hydride, *J. Chem. Phys.* 16 (11) (1948) 1077–1081, <https://doi.org/10.1063/1.1746727>.
- C.Y. Ho, R.W. Powell, P.E. Liley, Thermal conductivity of the elements, *J. Phys. Chem. Ref. Data* 1 (2) (1972) 279–421, <https://doi.org/10.1063/1.3253100>.
- D.E. Diller, Measurements of the viscosity of parahydrogen, *J. Chem. Phys.* 42 (6) (1965) 2089–2100, <https://doi.org/10.1063/1.1696250>.
- J.D. Rogers, F.G. Brickwedde, Comparison of saturated-liquid viscosities of low molecular substances according to the quantum principle of corresponding states, *Physica* 32 (6) (1966) 1001–1018, [https://doi.org/10.1016/0031-8914\(66\)90138-8](https://doi.org/10.1016/0031-8914(66)90138-8).

- [37] C.K. Briggs, R.G. Hickman, R.T. Tsugawa, P.C. Souers, Estimated viscosity, Surface tension, and Density of Liquid DT from the Triple Point to 25 K, Lawrence Livermore Lab., California Univ., Livermore (USA), 1975.
- [38] G. Cini-Castagnoli, A. Giardini-Guidoni, F.P. Ricci, Diffusion of neon, HT, and deuterium in liquid hydrogen, *Phys. Rev.* 123 (2) (1961) 404, <https://doi.org/10.1103/PhysRev.123.404>.
- [39] S.O. Kucheyev, A.V. Hamza, Condensed hydrogen for thermonuclear fusion, *J. Appl. Phys.* 108 (9) (2010) 091101, <https://doi.org/10.1063/1.3489943>.
- [40] A.B. Van Cleave, O. Maass, The viscosities of deuterium-hydrogen mixtures, *Can. J. Res.* 13 (6) (1935) 384–389, <https://doi.org/10.1139/cjr35b-039>.
- [41] H. Oh, M. Hirscher, Quantum sieving for separation of hydrogen isotopes using MOFs, *EurJIC* 2016 (27) (2016) 4278–4289, <https://doi.org/10.1002/ejic.201600253>.
- [42] A. Raza, S. Alafnan, G. Glatz, M. Arif, M. Mahmoud, et al., Hydrogen diffusion in organic-rich porous media: implications for hydrogen geo-storage, *Energy & Fuels* 36 (24) (2022) 15013–15022, <https://doi.org/10.1021/acs.energyfuels.2c03070>.
- [43] L.S. Darken, Diffusion, mobility and their interrelation through free energy in binary metallic systems, *Trans. AIME* 175 (1948) 184–201.
- [44] J.R. Gaines, P.A. Fedders, G.W. Collins, J.D. Sater, P.C. Souers, Diffusion of atoms and molecules in the solid hydrogens, *Phys. Rev. B* 52 (10) (1995) 7243, <https://doi.org/10.1103/PhysRevB.52.7243>.
- [45] D.M. Stefanescu, Diffusive Mass Transport At the Macroscale. In: Science and Engineering of Casting Solidification, Springer, Cham, 2015, p. 67, [https://doi.org/10.1007/978-3-319-15693-4\\_5](https://doi.org/10.1007/978-3-319-15693-4_5).
- [46] D.A. Porter, K.E. Easterling, Phase Transformations in Metals and Alloys (Revised Reprint), 3rd ed., CRC press, Boca Raton, 2009, p. 211, <https://doi.org/10.1201/9781439883570>.
- [47] X. Zhang, Y. Jia, L. Sheng, L. Yuan, J. Li, Characterization of segregation degree for large size metal component and application on high-speed train wheel, *Anal. Chim. Acta* 1203 (2022) 339719, <https://doi.org/10.1016/j.aca.2022.339719>.
- [48] P.J. García Nieto, V.M. Gonzalez Suarez, J.C. Álvarez Antón, et al., A new predictive model of centerline segregation in continuous cast steel slabs by using multivariate adaptive regression splines approach, *Materials* 8 (6) (2015) 3562–3583, <https://doi.org/10.3390/ma8063562>.
- [49] M. Waldrop, Plasma physics: the fusion upstarts, *Nature* 511 (2014) 398–400, <https://doi.org/10.1038/511398a>.
- [50] R.G. Guan, D. Tie, A review on grain refinement of aluminum alloys: progresses, challenges and prospects, *Acta Metall. Sin. (Engl. Lett.)* 30 (2017) 409–432.
- [51] K. Iwano, J. Zhang, A. Iwamoto, Y. Iwasa, K. Shigemori, Refractive index measurements of solid deuterium-tritium, *Sci. Rep.* 12 (1) (2022) 2223, <https://doi.org/10.1038/s41598-022-06298-1>.